Interdecadal Variations of the Silk Road Pattern

LIN WANG

Center for Monsoon System Research, and LASG, Institute of Atmospheric Physics, Chinese Academy of Sciences, Beijing, China

PEIQIANG XU

Center for Monsoon System Research, Institute of Atmospheric Physics, Chinese Academy of Sciences, and College of Earth Sciences, University of Chinese Academy of Sciences, Beijing, China

WEN CHEN AND YONG LIU

Center for Monsoon System Research, and LASG, Institute of Atmospheric Physics, Chinese Academy of Sciences, Beijing, China

(Manuscript received 22 May 2017, in final form 30 August 2017)

ABSTRACT

Based on several reanalysis and observational datasets, this study suggests that the Silk Road pattern (SRP), a major teleconnection pattern stretching across Eurasia in the boreal summer, shows clear interdecadal variations that explain approximately 50% of its total variance. The interdecadal SRP features a strong barotropic wave train along the Asian subtropical jet, resembling its interannual counterpart. Additionally, it features a second weak wave train over the northern part of Eurasia, leading to larger meridional scale than its interannual counterpart. The interdecadal SRP contributes approximately 40% of the summer surface air temperature's variance with little uncertainty and 10%–20% of the summer precipitation's variance with greater uncertainty over large domains of Eurasia. The interdecadal SRP shows two regime shifts in 1972 and 1997. The latter shift explains over 40% of the observed rainfall reduction over northeastern Asia and over 40% of the observed warming over eastern Europe, western Asia, and northeastern Asia, highlighting its importance to the recent decadal climate variations over Eurasia. The Atlantic multidecadal oscillation (AMO) does not show a significant linear relationship with the interdecadal SRP. However, the Monte Carlo bootstrapping resampling analysis suggests that the positive (negative) phases of the spring and summer AMO significantly facilitate the occurrence of negative (positive) phases of the interdecadal SRP, implying plausible prediction potentials for the interdecadal variations of the SRP. The reported results are insensitive to the long-term trends in datasets and thereby have little relevance to externally forced climate change.

1. Introduction

The Silk Road pattern (SRP) is a zonally oriented teleconnection pattern in the boreal summer that consists of several geographically fixed centers along the upper-tropospheric subtropical jet over the Eurasian continent (Lu et al. 2002; Enomoto et al. 2003; Kosaka et al. 2009). One of its phases features anomalous barotropic anticyclones (cyclones) over the Caspian Sea and Korean Peninsula (eastern Europe and Mongolia) (e.g., Ding and Wang 2005; Sato and Takahashi 2006; Kosaka et al. 2009; also see Figs. 1a–d), corresponding to significant precipitation and surface air temperature anomalies over Europe and Asia (e.g., Lu et al. 2002; Wu 2002; Enomoto et al. 2003; Ding and Wang 2005; Huang et al. 2011, 2012; Chen and Huang 2012; Saeed et al. 2011, 2014; Hong and Lu 2016; also see Figs. 1g and 1h).

The SRP was discovered during studies on the link between the Indian summer monsoon and the East Asian summer monsoon and on the formation of the Bonin high, which accounts for hot summers in Japan. The 200-hPa wind pattern, which resembles the SRP and has been referred to as the Asian continent pattern (Krishnan and Sugi 2001), was noticed by Lau et al. (2000) and Krishnan and Sugi (2001) when they studied the variations of the Indian summer rainfall and mei-yu

Corresponding author: Dr. Lin Wang, wanglin@mail.iap.ac.cn

DOI: 10.1175/JCLI-D-17-0340.1

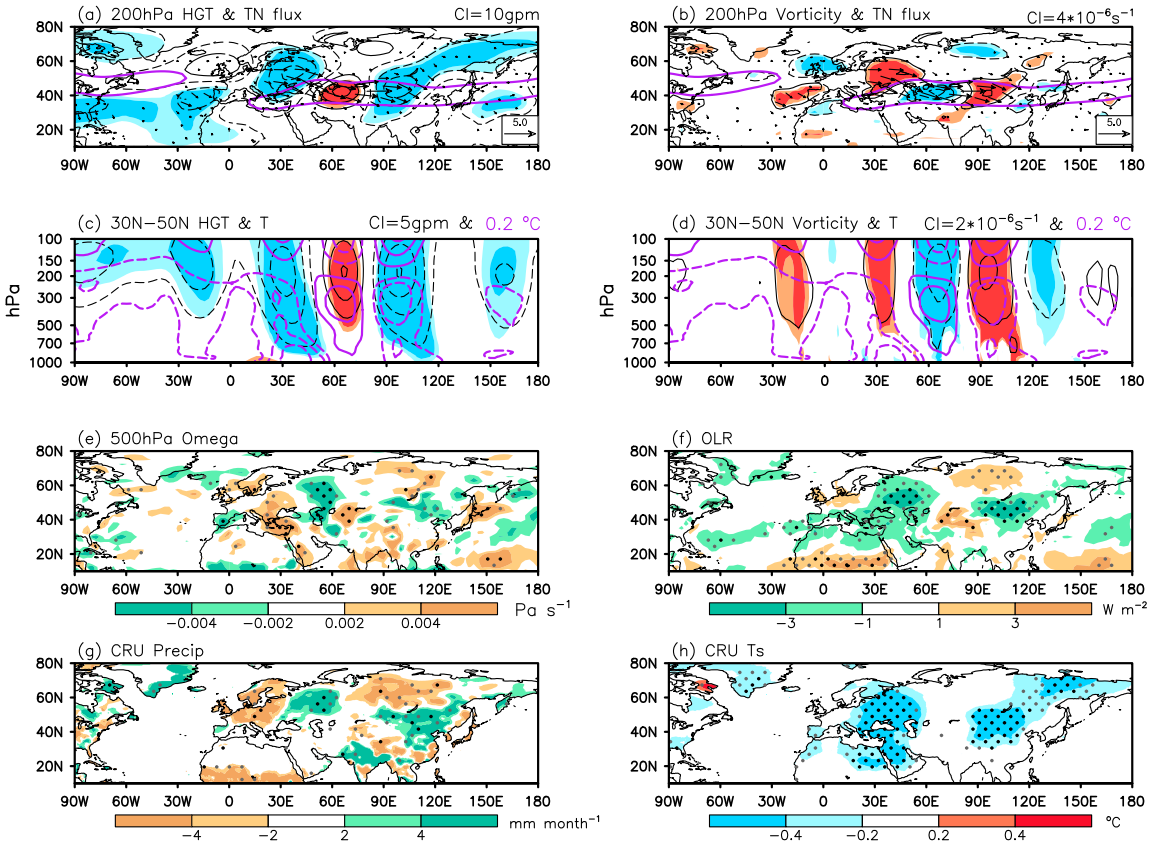

FIG. 1. (a) Summer mean 200-hPa geopotential height anomalies [black contour, contour interval (CI) = 10 gpm] and the horizontal component of the wave activity flux (arrow, unit: $m^2 s^{-2}$) associated with the SRP index, obtained via a linear regression overlaid by the climatology of the 200-hPa summer mean zonal wind, as indicated by the 20 m s^{-1} purple contour. (c) The regression of the 30°–50°N averaged summer mean geopotential height (black contour, CI = 5 gpm) and air temperature (purple contour, CI = 0.2°C) onto the SRP index. (b),(d) As in (a),(c), but geopotential height is replaced with relative vorticity [black contour; CI = 4 (±2, ±6, ±10, . . .) × 10^{-6} s^{-1} for (b) and CI = 2 (±1, ±3, ±5, . . .) × 10^{-6} s^{-1} for (d)]. Also shown are regression of the summer mean (e) 500-hPa vertical velocity [shading interval (SI) = 0.002 Pa s^{-1}], (f) OLR (SI = 2 W m^{-2}), (g) precipitation (SI = 2 mm $month^{-1}$), and (h) surface air temperature (SI = 0.2°C) onto the SRP index. The light and dark shading in (a)–(d) and the gray and black dots in (e)–(h) indicate the 95% and 99% confidence levels based on the two-tailed Student's *t* test, respectively. The SRP index and atmospheric variables are from the ERA-Interim dataset, and the precipitation and surface air temperature are from the CRU TS v4.00 dataset. The regression was applied to the period 1979–2013 for (f) and to the period 1979–2015 for the other plots.

rainfall, respectively. A similar wind pattern, which was called the midlatitude Asian summer pattern, was revealed by applying the multivariable empirical orthogonal function to the summer mean 200-hPa winds (Wu 2002). A study on the teleconnectivity of the 200-hPa meridional winds identified the existence of the SRP along the subtropical Asian westerly jet (Lu et al. 2002), and the analysis of Rossby wavenumbers confirmed its nature as a stationary Rossby wave trapped in the jet stream (Lu et al. 2002; Enomoto et al. 2003). Although the SRP, as Enomoto et al. (2003) called it, is mainly observed along the Asian subtropical jet stream, it is also believed to be able to propagate throughout the entire Northern Hemisphere and form a circumglobal teleconnection (CGT; Ding and Wang 2005).

The formation mechanism of the SRP has been a major issue since the discovery of the SRP. There is a strong consensus regarding the trapped feature of the SRP in the Asian subtropical jet, since the jet can serve as an efficient Rossby waveguide (Hoskins and Ambrizzi 1993; Ambrizzi et al. 1995). In contrast, a weaker consensus has been reached on the excitation and maintenance mechanism of the SRP. On the one hand, it is suggested that the SRP is an internal atmospheric mode because the spatial structure of the SRP can be well reproduced in a dry atmospheric model driven by either time-varying or long-term mean diabatic heating (Yasui and Watanabe 2010). The extraction of the kinetic and available potential energy from the basic flows via barotropic (Sato and Takahashi 2006) and baroclinic

(Kosaka et al. 2009; Chen et al. 2013) energy conversion processes is important to maintain the SRP, and the configuration of the mean flow determines the phase-locking feature of the SRP (Kosaka et al. 2009). On the other hand, atmospheric external forcing is also believed to play some role because atmospheric external factors, such as convections near the eastern Mediterranean (Yasui and Watanabe 2010), diabatic heating over the Indian summer monsoon region (Wu 2002; Enomoto et al. 2003; Enomoto 2004; Ding and Wang 2005; Ding et al. 2011) or the Indian Ocean (Chen and Huang 2012), and El Niño–Southern Oscillation (ENSO), could also excite the SRP and modulate its phases (Ding et al. 2011). Nevertheless, the relationship between the SRP and these external atmospheric factors could be vague or unstable (Lu et al. 2006; Yasui and Watanabe 2010; Kosaka et al. 2012; Wang et al. 2012). Moreover, the temporal variability of the SRP cannot be predicted by coupled climate models, although the spatial structure of the SRP can be well captured (Kosaka et al. 2012), suggesting the unpredictable features of the SRP on interannual time scale.

Compared with the extensively investigated interannual variability of the SRP, the interdecadal variations of the SRP have seldom been reported but have been implied in recent studies. For example, an upper-tropospheric wave pattern that resembles the SRP was observed accompanying the amplified summer warming in Europe, western Asia, and northeastern Asia (e.g., Hong et al. 2017) and the weakened summer precipitation over the Asian inland plateau region (e.g., Piao et al. 2017) and the lower reaches of the Yangtze River valley (e.g., Zhu et al. 2011, 2016; Si and Ding 2016) after the late 1990s. These results imply the existence of the SRP variability on decadal or longer time scales, but previous works have mainly used this SRP-like wave pattern to explain the observed climate anomalies and have not addressed the temporal features of the SRP itself. In fact, Chen and Huang (2012) noticed an interdecadal strengthening and weakening of the SRP index in approximately 1974 and 1997 (see their Fig. 5a), respectively, but they filtered out the interdecadal component and focused on the interannual variability. Hong et al. (2017) reported an interdecadal strengthening and weakening of the SRP index in approximately 1964 and 1997, which is partly consistent with Chen and Huang (2012). On the other hand, Wu et al. (2016) obtained an interdecadal CGT pattern via an analysis of the decadal-filtered geopotential height data. Clear differences exist between their interdecadal CGT patterns (see their Fig. 3) and the conventionally recognized SRP or CGT patterns (e.g., Fig. 5 of Ding and Wang 2005; Fig. 2a of Chen et al. 2013). These contrasting results motivate a careful investigation of both the temporal and spatial features of the interdecadal variations of the SRP. In addition, although the SRP and atmospheric external factors show vague links on interannual time scale, it remains unclear whether some atmospheric external forcing could lead to the preferred phase of the SRP on interdecadal time scale.

In this study, we investigate the spatial and temporal characteristics of the SRP as well as its associated climate anomalies on interdecadal time scale based on several reanalysis and observational datasets. Comparisons are made among different datasets and with the patterns on interannual time scale. A possible link with sea surface temperature (SST) is also discussed. Section 2 introduces the datasets and methodologies used in this study. Section 3 briefly describes the structure of the SRP and its associated climate anomalies. Section 4 shows the variations of the SRP on interdecadal time scale and compares them with those on interannual time scale. Section 5 quantifies the association of the interdecadal variations of the SRP to the shift of Eurasian summer climate in the late 1990s, and section 6 links the interdecadal variability of the SRP to the SST. Finally, section 7 summarizes the key findings and discusses some remaining issues.

2. Data and methods

The monthly mean atmospheric reanalysis data used in this study are from several sources, including the ERA-Interim dataset (Dee et al. 2011), the National Centers for Environmental Prediction (NCEP)–National Center for Atmospheric Research (NCAR) reanalysis dataset (Kalnay et al. 1996), the Japanese 55-year Reanalysis (JRA-55) dataset (Kobayashi et al. 2015), the European Centre for Medium-Range Weather Forecasts (ECMWF) Twentieth Century Reanalysis (ERA-20C) dataset (Poli et al. 2016), and the Twentieth Century Reanalysis dataset, version 2c (20CRV2c; Compo et al. 2011). The monthly mean precipitation and surface air temperature data are from the University of Delaware (UDEL) air temperature and precipitation dataset, version 4.01 (Willmott and Matsuura 2014) and the Climatic Research Unit (CRU) high-resolution gridded datasets, version 4.00 (CRU TSv4.00, Harris et al. 2014). The interpolated monthly mean outgoing longwave radiation (OLR) data are from the National Oceanic and Atmospheric Administration (NOAA) and serve as a proxy for convection (Liebmann and Smith 1996). The SST data are from the monthly mean Extended Reconstructed Sea Surface Temperature (ERSST) dataset, version 4 (Huang et al.

TABLE 1. Datasets used in this study.

Dataset	Resolution	Period of record
ERA-Interim reanalysis	2.5° × 2.5°	1979–2015
JRA-55 reanalysis	1.25° × 1.25°	1958–2015
NCEP–NCAR reanalysis	2.5° × 2.5°	1948–2015
ERA-20C reanalysis	2.5° × 2.5°	1900–2010
20CRV2c reanalysis	2° × 2°	1851–2011
NOAA interpolated OLR	2.5° × 2.5°	1979–2013
UDEL v4.01	0.5° × 0.5°	1900–2014
CRU TS v4.00	0.5° × 0.5°	1901–2015
ERSST.v4	2° × 2°	1854–2016
PDO index	—	1900–2016
AMO index	—	1880–2016

2015). The Pacific decadal oscillation (PDO; Mantua et al. 1997) index and the Atlantic multidecadal oscillation (AMO; Schlesinger and Ramankutty 1994) index were downloaded from http://research.jisao.washington.edu/pdo/PDO.latest.txt and http://climexp.knmi.nl/data/iamo_ersst.dat, respectively. A brief summary of these data is given in Table 1.

The summer mean is defined as the average of June, July, and August (JJA) and is used throughout this study except where otherwise stated explicitly. The SRP pattern is defined as the first empirical orthogonal function (EOF) mode of the summer mean 200-hPa meridional wind over the domain (20°–60°N, 30°–130°E; Kosaka et al. 2009), and the SRP index is defined as the normalized first principal component accordingly. To maintain consistency and for easy comparisons among the datasets with consideration for their different temporal coverages, the SRP pattern was extracted by applying EOF analysis to the overlapping periods of different datasets (i.e., 1979–2010), and the SRP index was obtained by projecting the SRP pattern onto the 200-hPa meridional wind anomalies of the whole period of each dataset. We also tried to obtain the SRP pattern and index by applying EOF analysis to slightly different domains (e.g., Chen and Huang 2012; Hong et al. 2017) or different time periods, and the results are insensitive to these slight changes. The interdecadal component of a variable is extracted using a 9-yr Lanczos low-pass filter, and the interannual component is defined as the residual of the original variable minus its interdecadal component. The confidence level of the linear regression is evaluated using the two-tailed Student's t test, and the effective degree of freedom ($N_{\rm dof}$) is evaluated following Bretherton et al. (1999):

$$N_{\rm dof} = N(1 - r_1 r_2)/(1 + r_1 r_2),$$

where N is the sample size and r_1 and r_2 are the lag-1 autocorrelations of the two time series. Considering there are very few oceanic observations before 1920 (Dai 2013), this study only considers the period after 1920.

3. Overview of the SRP

Figures 1a–d show the SRP obtained using a linear regression onto the SRP index based on the ERA-Interim data during the period 1979–2015. A clear wave train–like structure is observed in the upper troposphere, with three anticyclonic centers over the British Isles, Caspian Sea, and Korean Peninsula and two cyclonic centers over eastern Europe and Mongolia. The wave train–like structure is equivalent barotropic and tilts slightly westward with height in the troposphere, with the maximum amplitude located near the tropopause (between 200 and 150 hPa). Cold (warm) anomalies are observed below (above) the cyclonic maximum, and warm (cold) anomalies are observed below (above) the anticyclonic maximum (Figs. 1c,d). This geopotential/relative vorticity–temperature configuration is similar to many wintertime wave patterns (e.g., Fig. 3 of Park et al. 2011, Fig. 6 of Song et al. 2016, Fig. 4 of Hu et al. 2017) and indicates the thermal wind balance ($\partial\zeta/\partial z \propto -\partial\Phi'/\partial z \propto -T'$) of the SRP. In addition, the SRP-related temperature anomalies are located slightly westward of the geopotential height and relative vorticity anomalies (Figs. 1c,d), indicating that the structure of the SRP allows for the efficient meridional heat exchange via eddy heat flux. Hereafter, we refer to the phase shown in Figs. 1a–d as the positive phase of the SRP.

The wave activity flux (Takaya and Nakamura 2001) associated with the SRP emanates from Europe, enters the Asian jet stream near the Caspian Sea, and points continuously eastward toward East Asia along the jet stream, confirming that the SRP is a Rossby wave train. The anticyclonic centers over the British Isles and Korean Peninsula are relatively weak and insignificant in the geopotential height field (Figs. 1a,c), but they are clear and significant in the relative vorticity field (Figs. 1b,d). Meanwhile, the clear wave activity fluxes emanate from the anticyclonic (cyclonic) center over the British Isles (Mongolia) toward the cyclonic (anticyclonic) center over the Caspian Sea (Korean Peninsula) (Figs. 1a and 1b). In contrast, although the cyclonic center to the east of Japan is significant in both the geopotential height and relative vorticity fields, the wave activity fluxes pointing to this center are very weak. On one hand, this result suggests that the SRP is mainly observed from the British Isles to the Korean Peninsula and that it decays rapidly outside of Eurasia. On the other hand, the differences between Figs. 1a and 1b suggest that, compared with geopotential

height, relative vorticity may better delineate the structure of the SRP, which is consistent with the argument that relative vorticity has some advantages over geopotential height in representing the two-dimensional propagation of Rossby waves (Hoskins et al. 1977).

In the downstream portion of the SRP, an enhanced ascending motion is observed to the east of the anomalous barotropic cyclone over Mongolia (Fig. 1e) in the positive phase of the SRP, facilitating enhanced convection (Fig. 1f) and precipitation (Fig. 1g) over northeast China and Mongolia. Meanwhile, large-scale surface cooling extends from north of the Tibetan Plateau to eastern Siberia (Fig. 1h), corresponding well to the southwest–northeast-oriented cyclonic anomalies over Mongolia (Figs. 1a,b). The configuration of the circulation and temperature (Figs. 1c,d) suggests that the cooling is induced by the anomalous cold advection from higher latitudes occurring in the western portion of the anomalous cyclone. In the upstream portion of the SRP, similar configurations can also be observed. That is, ascending (descending) motions and enhanced (weakened) precipitation are located to the east (west) of the anomalous cyclone over eastern Europe, and large-scale surface cooling is observed directly below the anomalous cyclone.

4. Interdecadal variations of the SRP

a. Temporal features

Figure 2 shows the SRP index and its interdecadal component in five reanalysis datasets. Before any analysis is performed, we first check the consistency of the SRP variability represented by the different datasets by calculating the correlation coefficients of the SRP indexes among the datasets (Table 2). This analysis reveals that both the interannual and interdecadal variability of the SRP are almost identical to each other in the ERA-Interim, JRA-55, and NCEP–NCAR datasets, with all the correlation coefficients exceeding 0.99 for the 1979–2010 and 1958–2010 periods. The SRP variability in the ERA-20C dataset is highly consistent with those in the ERA-Interim, JRA-55, and NCEP–NCAR datasets, with correlation coefficients on the order of 0.9 or higher during their overlapping periods. In contrast, the SRP variability in the 20CRV2c dataset is less consistent with those in the other datasets, such that the correlation coefficients are generally on the order of 0.8 or lower during their overlapping periods. Therefore, the following analyses are mainly based on the ERA-Interim, JRA-55, NCEP–NCAR and ERA-20C datasets, while that based on the 20CRV2c dataset is used only for reference.

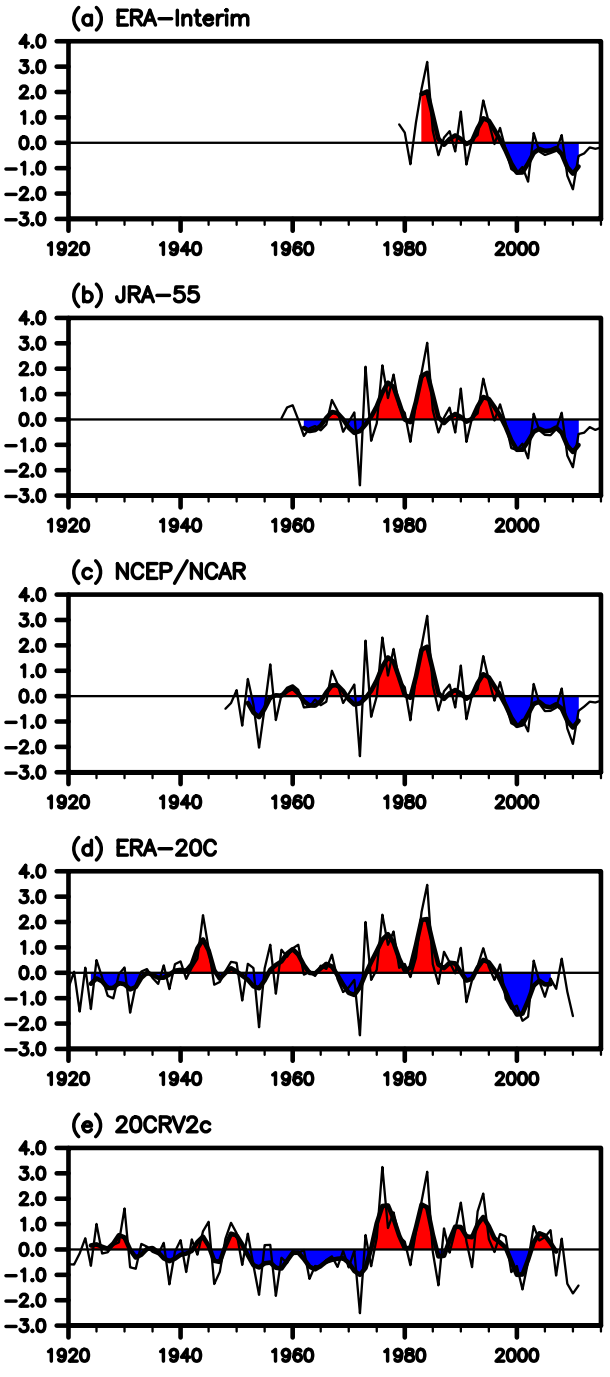

FIG. 2. The normalized SRP index (thin line) and its interdecadal component (thick line with filled colors) in the (a) ERA-Interim, (b) JRA-55, (c) NCEP–NCAR, (d) ERA-20C, and (e) 20CRV2c datasets.

A remarkable feature of the SRP index is that it is in the interdecadal positive phase from the mid-1970s to the late 1990s and that it switches to its interdecadal negative phase after approximately 1998 (Figs. 2a–d). The SRP index also shows clear low-frequency variability

TABLE 2. Correlation coefficients of the original, interdecadal, and interannual (left to right, separated by slashes) SRP indexes among the different datasets for the periods 1979–2010, 1958–2010, and 1948–2010. All of the correlation coefficients exceed the 99.9% confidence level based on two-tailed Student's *t* test.

1979–2010	20CRV2c	NCEP–NCAR	JRA-55	ERA-Interim
ERA-20C	0.81/0.82/0.77	0.94/0.97/0.89	0.93/0.95/0.87	0.94/0.97/0.91
20CRV2c	—	0.84/0.87/0.67	0.83/0.87/0.65	0.84/0.88/0.64
NCEP–NCAR	—	—	1.00/1.00/1.00	1.00/1.00/1.00
JRA-55	—	—	—	1.00/1.00/1.00
1958–2010	**20CRV2c**	**NCEP–NCAR**	**JRA-55**	
ERA-20C	0.76/0.67/0.81	0.92/0.91/0.93	0.92/0.93/0.94	
20CRV2c	—	0.80/0.79/0.76	0.80/0.83/0.74	
NCEP–NCAR	—	—	0.99/0.99/1.00	
1948–2010	**20CRV2c**	**NCEP–NCAR**		
ERA-20C	0.76/0.66/0.83	0.92/0.91/0.93		
20CRV2c	—	0.80/0.79/0.78		

before the mid-1970s, but the magnitude of this variability is smaller than that after the mid-1970s (Figs. 2b–d). This feature remains the same when the linear trends are removed from the data (not shown), indicating that it is not externally forced by, say, global warming. To illustrate the variability of the SRP in more detail, Morlet wavelet analyses (Torrence and Compo 1998) was applied to the SRP indexes of the five datasets. The global wavelet spectrum indicates that the SRP has clear peaks of 8–16-yr and 32–64-yr variabilities in the five datasets (Figs. 3a–e), the former of which is mainly dominant after the 1960s, as revealed in the local wavelet power spectra. The global wavelet spectrum also shows peaks of 2–4- and 4–8-yr variabilities, but this feature is only significant in the ERA-Interim and 20CRV2c datasets. The local wavelet power spectrum indicates that the SRP variabilities with periods shorter than 16 years are weak before the 1960s compared with those after the 1960s (Figs. 3a–e). This distinct contrast may arise from the intrinsic feature of the SRP itself, but it may also arise from the uncertainty of the data especially before the 1940s. To reveal the possible regime shifts in the mean of the SRP index, a moving *t* test with a 13-yr window was applied to the SRP index. Two shift points are identified in 1972 and 1997 and are highly consistent in the five datasets (Figs. 3f–j). In addition, a shift point occurring in the 1930s is detected in the ERA-20C dataset but is missing in the 20CRV2c dataset, implying the uncertainty of its existence.

The variance explained by the interdecadal and interannual components of the SRP was examined to further illustrate the importance of the interdecadal variability of the SRP. The interdecadal component of the SRP generally explains over 50% of the total variance during the period 1979–2010 (Table 3). This ratio differs among the datasets, such that the highest values exceed 60% and are observed in the ERA-20C and ERA-Interim datasets. The ratio decreases slightly when the period is extended backward but still exceeds 48% in the ERA-20C dataset, even when the period extends back to 1920. In contrast, the variance explained by the interannual component of the SRP is only on the order of 25% of the variance during the period 1979–2010. This number increases when the period extends backward but remains lower than that explained by the interdecadal component of the SRP. These results suggest that interdecadal variability is a very important component of the SRP variability. In addition, the decreased variance explained by the interdecadal SRP when the data are traced back to the 1920s is consistent with Fig. 2, which shows that the magnitudes of the interdecadal components of the SRP before the mid-1970s are smaller than those afterward (Figs. 2b–d). Again, the results in the 20CRV2c dataset are different from those in the other datasets, especially during the period 1979–2010. Note that the data in the 20CRV2c dataset are an ensemble mean of 56 members (Compo et al. 2011), whereas those in the ERA-20C dataset are from a single member (Poli et al. 2016). Ensemble averaging could suppress the internal atmospheric variability significantly and lead to weaker variability, especially in the earlier periods when the reanalysis is not strongly constrained by observations. This might explain the above discrepancies between the 20CRV2c dataset and the other datasets.

b. *Spatial structures and associated climate anomalies*

To delineate the structures and associated climate anomalies of the interdecadal variations of the SRP, the interdecadal SRP index is regressed onto the interdecadal components of meteorological variables. These results are then compared with those associated with their interannual counterparts. Recall that

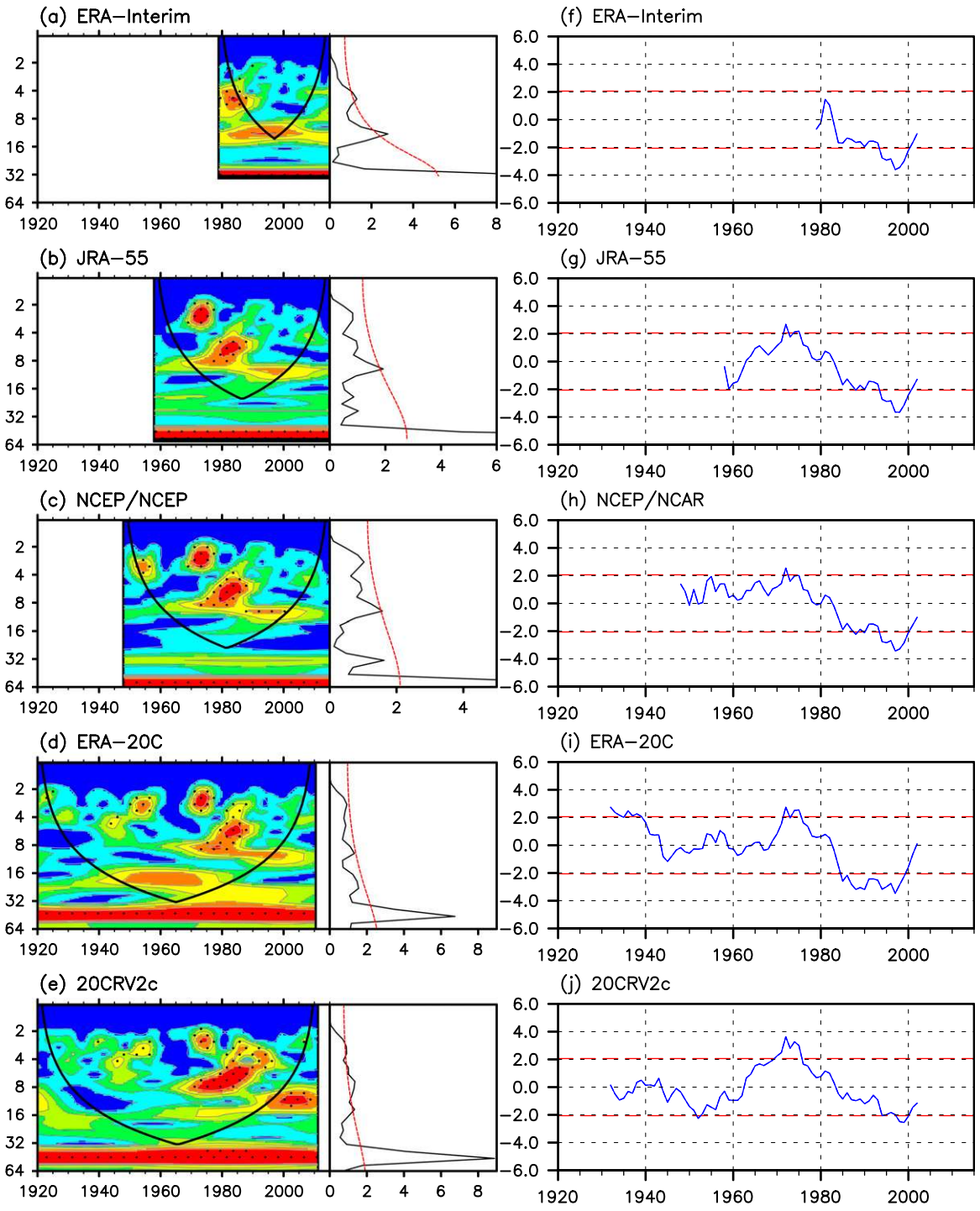

FIG. 3. (left) Local wavelet power spectra and global wavelet spectra of the SRP index based on Morlet wavelets in the (a) ERA-Interim, (b) JRA-55, (c) NCEP–NCAR, (d) ERA-20C, and (e) 20CRV2c datasets. (right) The t value of the moving t test on the mean of the SRP index with a 13-yr window in the (f) ERA-Interim, (g) JRA-55, (h) NCEP–NCAR, (i) ERA-20C, and (j) 20CRV2c datasets. Dots and dashed red curves in (a)–(e) indicate the 90% confidence level, and the dashed red lines in (f)–(j) indicate the 95% confidence level.

TABLE 3. Variance explained by the interdecadal and interannual (left and right, separated by a slash) components of the SRP index (unit: %) in the different datasets during the periods 1979–2010, 1958–2010, 1948–2010, and 1920–2010.

	ERA-20C	20CRV2c	NCEP–NCAR	JRA-55	ERA-Interim
1979–2010	64.5/25.2	35.1/34.8	53.8/27.2	55.2/26.6	60.7/26.1
1958–2010	54.6/34.4	47.8/35.5	44.1/42.1	48.2/44.9	—
1948–2010	49.6/40.2	46.0/37.7	43.3/46.7	—	—
1920–2010	48.6/40.0	43.0/42.8	—	—	—

the interdecadal component of an index or variable is extracted using a 9-yr Lanczos low-pass filter, and the interannual component is defined as the residual of the original index or variable minus its interdecadal component.

Figure 4 illustrates the SRP in the ERA-20C dataset for the period 1920–2010. Generally, the interdecadal SRP is also a zonally oriented barotropic wave train along the Asian jet stream (Figs. 4a–d) whose structure closely resembles the interannual SRP (Figs. 4e–h) and the overall SRP of the period 1979–2015, without distinguishing between the interdecadal and interannual components (Figs. 1a–d). A closer inspection reveals several structural differences between the interdecadal and interannual SRPs. First, the meridional scale of the interannual SRP covers approximately 20 latitudinal degrees, whereas that of the interdecadal SRP covers nearly 40 latitudinal degrees, especially stretching over eastern Europe and Mongolia. This feature can be seen in both the geopotential height (Figs. 4a,e) and the relative vorticity fields (Figs. 4c,g). Second, corresponding to the small meridional scale, the interannual SRP behaves as a Rossby wave train that is trapped in the subtropical Asian jet stream, as indicated by the wave activity fluxes (Figs. 4e,g). In contrast, the interdecadal SRP not only corresponds to the strong wave train along

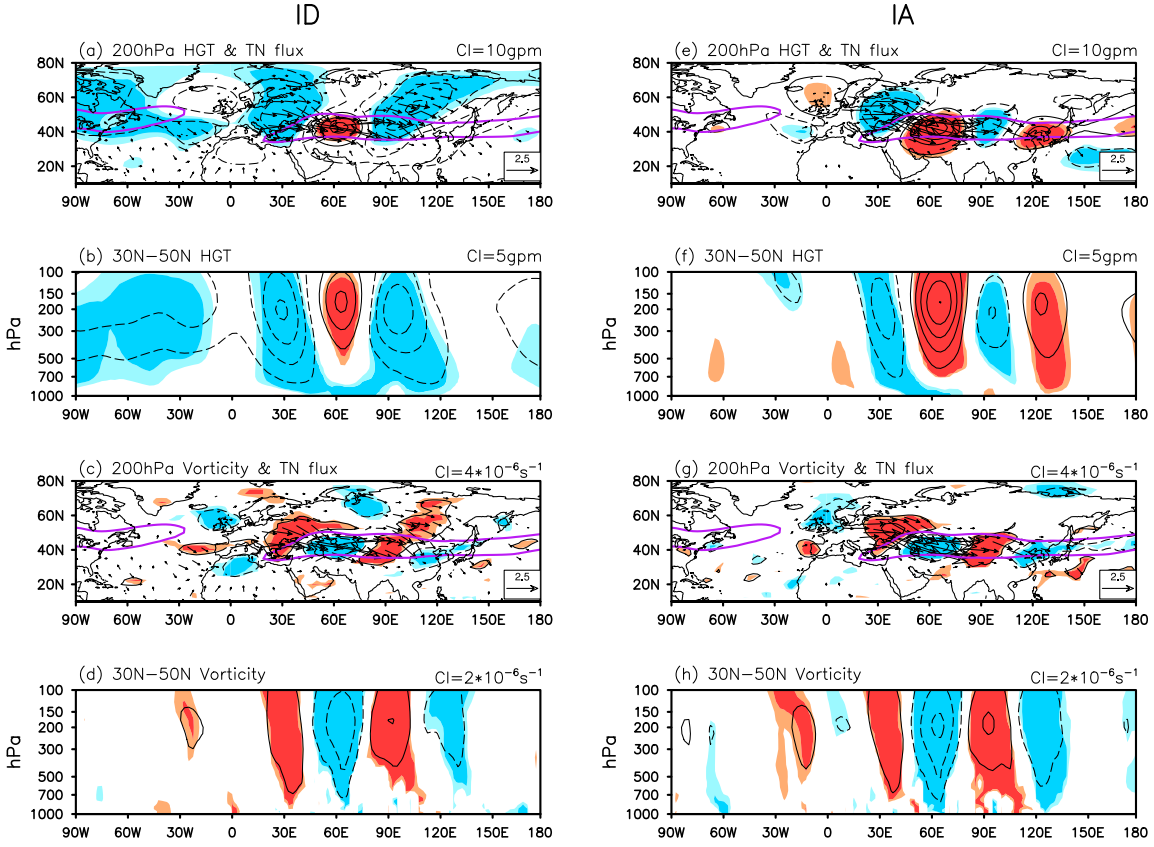

FIG. 4. (a)–(d) As in Figs. 1a–d, but based on the interdecadal components of the SRP index and the atmospheric variables from the ERA-20C dataset during the period 1920–2010. (e)–(h) As in (a)–(d), but based on the interannual components of the SRP index and the atmospheric variables.

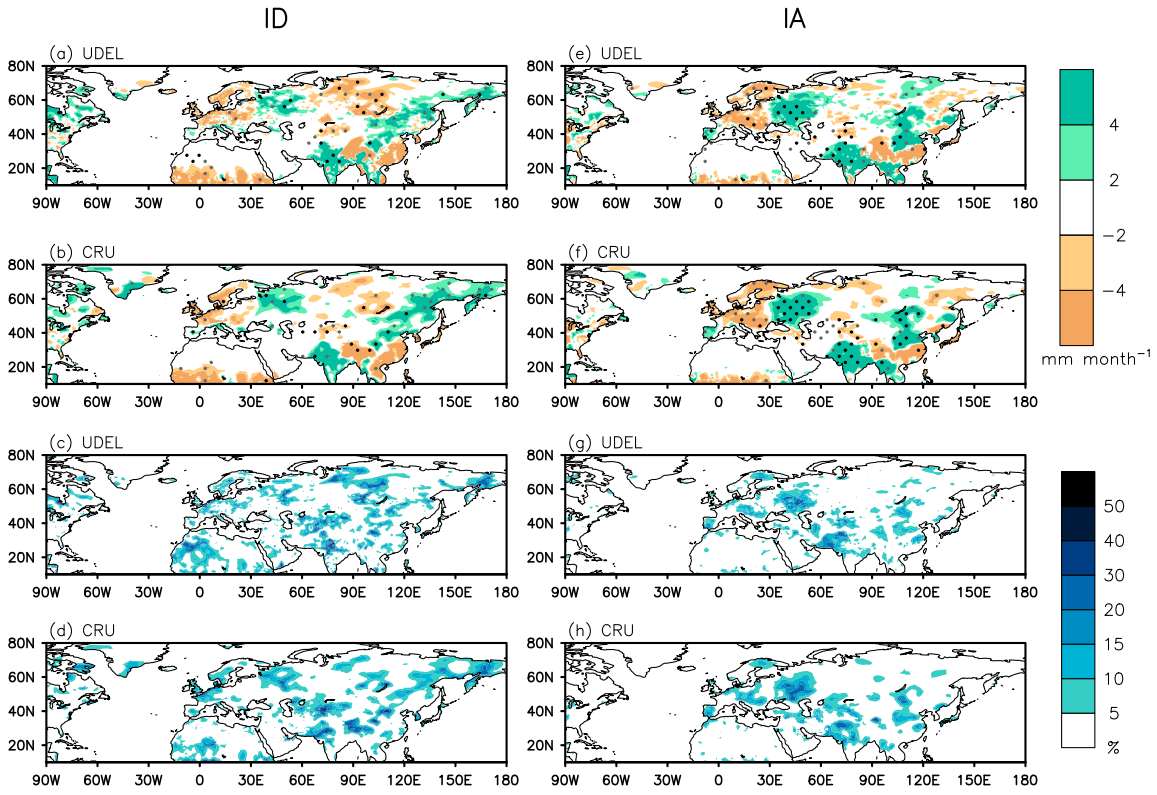

FIG. 5. (a),(b) Regression of the interdecadal component of the summer mean precipitation (unit: mm month $^{-1}$) from the UDEL v4.01 and CRU TS v4.00 datasets, respectively, onto the interdecadal SRP index from the ERA-20C dataset during the period 1920–2010. (c),(d) The variance of the precipitation explained by the interdecadal SRP index (unit: %) in the UDEL v4.01 and CRU TS v4.00 datasets, respectively, during the period 1920–2010. (e)–(h) As in (a)–(d), but based on the interannual components of the SRP index and precipitation. The SI are indicated in the legends beside the plots. The gray and black dots in (a), (b), (e), and (f) indicate the 95% and 99% confidence levels based on two-tailed Student's *t* test, respectively.

the subtropical Asian jet stream but also features a second branch of the wave train emanating from the British Isles, across northern Scandinavia and the Taymyr Peninsula, to Mongolia (Figs. 4a,c). Although this northern branch of the wave train is much weaker than its southern counterpart and is somewhat difficult to identify in the geopotential height field (Fig. 4a), it is clearer in the relative vorticity field (Fig. 4c). In fact, the large meridional scale of the interdecadal SRP can be attributed to the existence of this northern branch of wave train. Compared with the different horizontal structures, the vertical structures of the interannual and interdecadal SRPs are much alike and show fewer differences (Figs. 4b,d,f,h).

The formation of the northern branch of the wave train on an interdecadal time scale is likely related to the Rossby waveguide along the polar front jet (e.g., Figs. 3 and 4 of Iwao and Takahashi 2008). In fact, a similar wave train was also observed along the northern rim of the Eurasian continent on intraseasonal time scale in the boreal summer but has been accompanied by a counterpart wave train along the midlatitude subtropical jet stream in some cases (e.g., Iwao and Takahashi 2008) and not in others (e.g., Nakamura and Fukamachi 2004). The appearance of this wave train on interdecadal time scale might arise from the efficient modulation of the interdecadal background flow on a preferred phase of the intraseasonal wave train, and the disappearance of the wave train on interannual time scale might arise from cancellations between positive and negative phases of the intraseasonal wave train.

The rainfall anomalies associated with the interdecadal SRP based on the period 1920–2010 (Figs. 5a,b) are generally similar to those associated with the interannual SRP (Figs. 5e,f) and those associated with the overall SRP (i.e., without distinguishing the interdecadal and interannual components) from the period 1979–2015 (Fig. 1g). Reduced (enhanced) rainfall is observed over western Europe, Siberia, and the southern part of China (eastern Europe, India, and northeastern Asia) in the positive phase of the SRP (Figs. 5a,b,e,f). One slight difference is that the

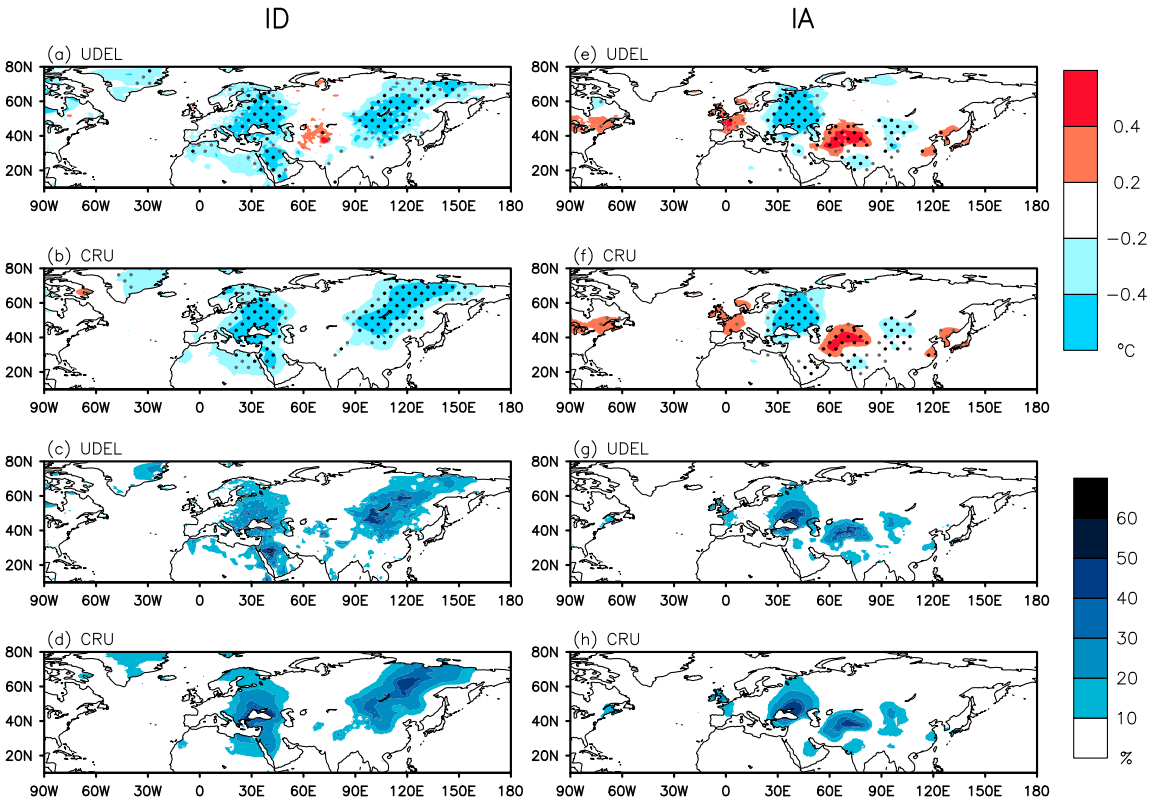

FIG. 6. As in Fig. 5, but for the surface air temperature (unit: °C).

interdecadal SRP-related enhanced rainfall over northeastern Asia extends from northern China to eastern Siberia (Figs. 5a,b) and shows a much larger meridional scale than the interannual SRP-related ones (Figs. 5e,f). This feature is consistent with the large meridional scale of the interdecadal SRP over East Asia (Fig. 4). On the other hand, significant wavelike rainfall anomalies stretching from India northeastward to northern China are observed on interannual time scale (Figs. 5e,f). Similar rainfall anomalies are also observed on interdecadal time scale, but the signals are less significant (Figs. 5a,b). This result suggests that the SRP is an important mechanism linking the variability of the Indian summer rainfall and the East Asian summer rainfall on interannual time scales (e.g., Lau et al. 2000; Krishnan and Sugi 2001; Lu et al. 2002; Ding and Wang 2005; Wu et al. 2016) and that its role is similar but weaker on interdecadal time scales. Note that, although the SRP-related rainfall shows well-defined patterns on both interannual and interdecadal time scales, the amount of the variance of the rainfall explained by the SRP is only on the order of 10%–20% (Figs. 5c,d,g,h).

The positive phase of the interdecadal SRP features large-scale cooling over Europe, western Asia, and northeastern Asia and weak warming over central Asia (Figs. 6a,b), consistent with Sutton and Dong (2012) and Hong et al. (2017). The variance of the surface air temperature explained by the interdecadal SRP generally exceeds 20%, and reaches up to 50% over eastern Europe, western Asia, and northeastern Asia, suggesting that the SRP is an important factor that modulates the surface air temperature over the Eurasian continent on interdecadal time scales. In contrast, the positive phase of the interannual SRP features cooling over eastern Europe and western Mongolia and warming over western Europe, central Asia, and temperate East Asia (Figs. 6e,f). The amount of the variance of the surface air temperature explained by the interannual SRP is large (20%–50%) over eastern Europe, central Asia, and western Mongolia and small over northeastern Asia (Figs. 6g,h), in remarkable contrast to the results on interdecadal time scale (Figs. 6c,d). Again, these differences are closely related to the different structures of the interannual and interdecadal SRPs (Fig. 4).

5. Role in the decadal shift of the Eurasian summer climate in the late 1990s

The interdecadal SRP was shown to accompany clear precipitation and temperature anomalies over East Asia

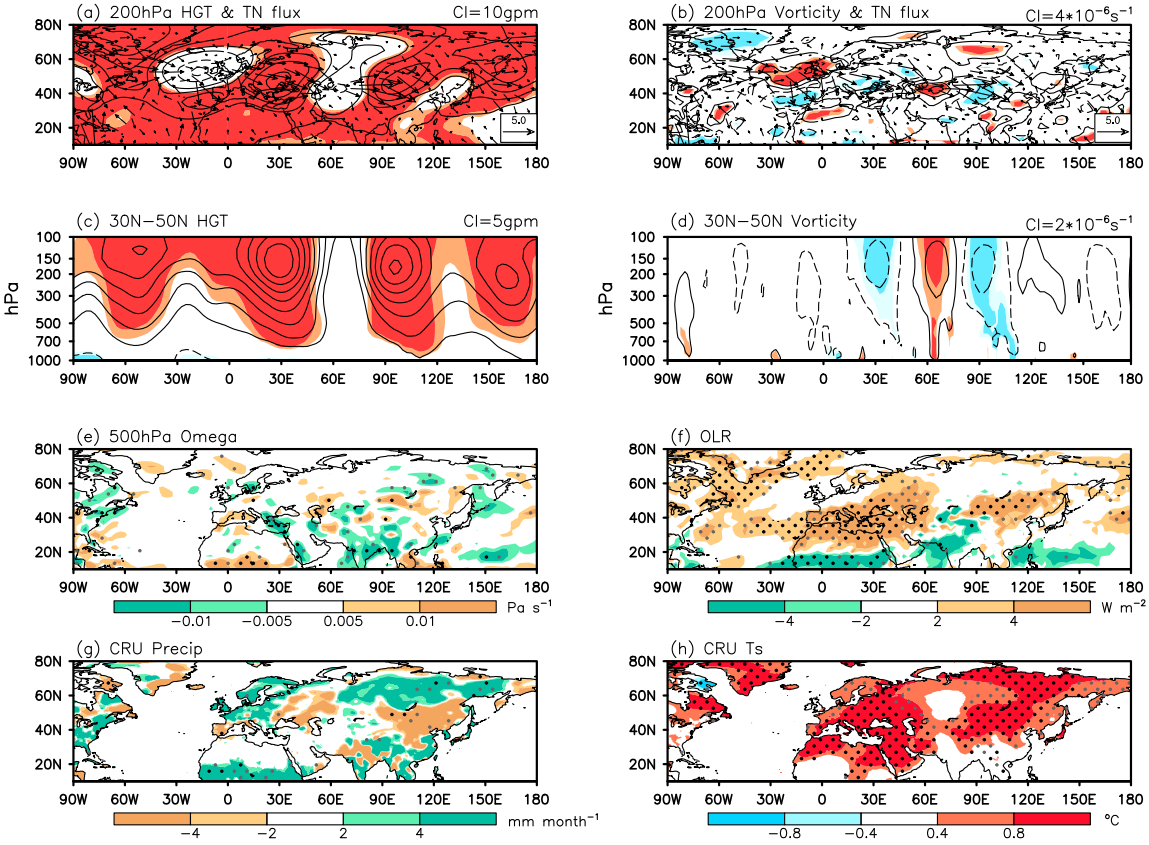

FIG. 7. Composite differences of the summer mean variables between the periods 1998–2015 [1998–2013 for (f)] and 1979–97. (a) 200-hPa geopotential height (contour; CI = 10 gpm) and associated wave activity flux (arrow; unit: $m^2 s^{-2}$), (b) 200-hPa relative vorticity [contour; CI = 4 (± 2, ± 6, ± 10, ...) $\times 10^{-6} s^{-1}$] and its associated wave activity flux (arrow, unit: $m^2 s^{-2}$), 30°–50 °N averaged, (c) geopotential height (CI = 5 gpm) and (d) relative vorticity [CI = 2 (± 1, ± 3, ± 5, ...) $\times 10^{-6} s^{-1}$], (e) 500-hPa vertical velocity (SI = 0.005 Pa s^{-1}), (f) OLR (SI = 2 W m^{-2}), (g) precipitation (SI = 2 mm $month^{-1}$), and (h) surface air temperature (SI = 0.2°C). The atmospheric variables are from the ERA-Interim dataset, and the precipitation and surface air temperature are from the CRU TS v4.00 dataset. The light and dark shading in (a)–(d) and the gray and black dots in (e)–(h) indicate the 95% and 99% confidence levels based on two-tailed Student's *t* test, respectively.

(section 4) and to transit from its interdecadal positive phase to its interdecadal negative phase in the late 1990s (Figs. 2 and 3f–j). Meanwhile, the East Asian summer monsoon and the European summer climate also show clear decadal shifts in the late 1990s (e.g., Huang et al. 2012, 2013; Sutton and Dong 2012; Chen and Lu 2014; Zhang 2015; Chen et al. 2016). Considering the almost simultaneous occurrence of these phenomena, it is natural to explore whether and to what extent the interdecadal variations of the SRP contribute to the decadal shifts of the Eurasian summer climate in the late 1990s.

Figure 7 shows the composite anomalies of several variables between the periods 1998–2015 and 1979–97. A wavelike pattern that resembles the negative phase of the SRP is observed in the troposphere, with a significant barotropic anticyclonic anomaly over Mongolia (Figs. 7a–d). The region dominated by this anomalous anticyclone is characterized by strong descending anomalies (Fig. 7e), suppressed convections (Fig. 7f), decreased precipitation (Fig. 7g), and large-scale warming (Fig. 7h). All of these features are consistent with the decadal shifts of the East Asian summer monsoon in the late 1990s (e.g., Huang et al. 2013; Si and Ding 2016; Hong et al. 2017). In addition, an anomalous anticyclone is observed over eastern Europe, corresponding to an anomalous descending motion (Fig. 7e) and weakened precipitation (Fig. 7g) over eastern Europe and enhanced precipitation over northwestern Europe (Fig. 7g), which is consistent with Sutton and Dong (2012). The clear similarities of Fig. 7 and Fig. 1 imply that the decadal shifts of the Eurasian summer climate in the late 1990s are very likely associated with the interdecadal variations of the SRP.

To quantitatively evaluate how much the decadal shifts of the Eurasian summer climate in the late 1990s are related to the SRP, the following procedure is used.

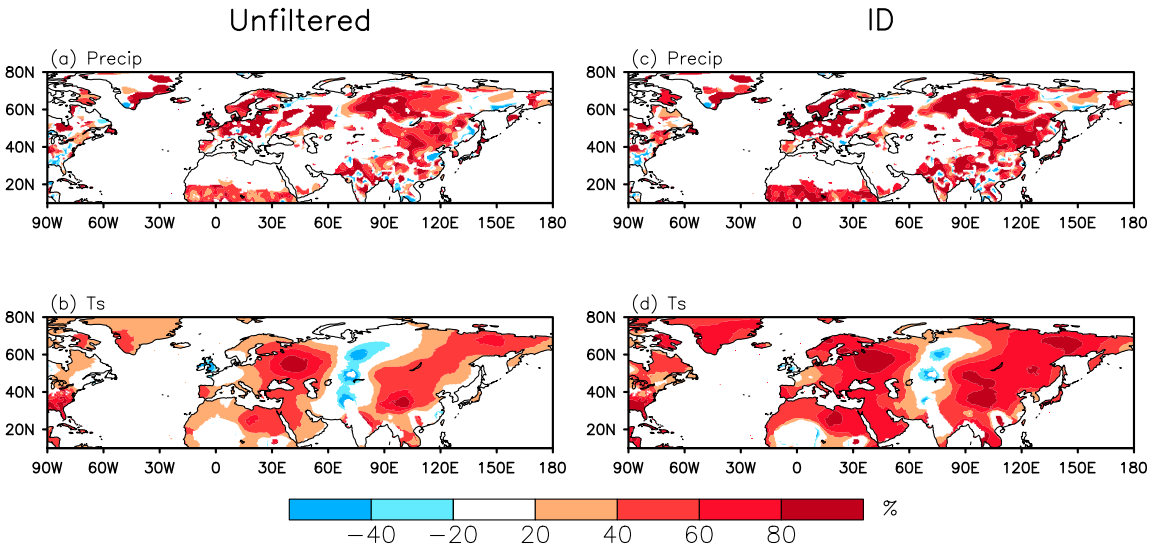

FIG. 8. The contribution of the SRP without distinguishing the interdecadal and interannual components to the decadal shift of the (a) precipitation and (b) surface air temperature in the late 1990s (unit: %). (c),(d) As in (a),(b), but for the contributions of the interdecadal SRP. The data are from the CRU TS v4.00 dataset. The positive and negative values indicate constructive and destructive contributions, respectively.

First, the SRP-related precipitation and surface air temperature anomalies (A_{SRP}) are calculated as follows:

$$A_{SRP} = I_{SRP} \times P_{SRP},$$

where I_{SRP} denotes the changes of the normalized SRP index between 1998–2015 and 1979–97, and P_{SRP} denotes the pattern of precipitation or surface air temperature corresponding to one standard deviation of the SRP index, which is obtained via a linear regression based on the period 1979–2015. Second, the SRP-related precipitation or surface air temperature anomalies (A_{SRP}) are divided by the observed decadal shifts of precipitation and surface air temperature (A_{OBS}; Figs. 7g,h) to obtain the ratio of the observed decadal change explained by the SRP (C_{SRP}):

$$C_{SRP} = A_{SRP}/A_{OBS} \times 100\%,$$

where C_{SRP} indicates the ratio of the observed decadal changes explained by the original/interannual/interdecadal SRP when A_{SRP} is calculated using the original/interannual/interdecadal index (I_{SRP}) and the pattern (P_{SRP}) of the SRP.

Figure 8 shows the spatial pattern of C_{SRP} for precipitation and the surface air temperature. It reveals that the SRP explains over 40% of the observed rainfall reduction over northeastern Asia (Figs. 8a and 7g) and that the ratio generally exceeds 60% (and even exceeds 80% over some regions of northeast China) when the interdecadal component of the SRP is considered alone (Fig. 8c). Also, C_{SRP} associated with the interannual component of the SRP was examined and was generally below 10% (not shown). In addition, the SRP explains more than 40% and 70% of the observed rainfall increase over northern central Siberia and northwestern Europe (Figs. 8a,c), respectively, where the decadal wetting anomalies are observed in the late 1990s (Fig. 7g). These results suggest that the decadal shift of the Eurasian summer precipitation in the late 1990s is substantially related to the interdecadal variations of the SRP.

In terms of the surface air temperature, the SRP explains over 40% of the observed decadal warming over eastern Europe, western Asia, North Africa, and the large areas extending from Tibetan Plateau northeastward to eastern Siberia (Figs. 8b and 7h). The ratio generally exceeds 60% when the interdecadal component of the SRP is considered alone (Fig. 8d). Additionally, the SRP contributes approximately 50% of the observed decadal cooling surrounding Lake Balkhash and counteracts approximates 30% of the observed decadal warming over central Asia and western Siberia (Figs. 7h, 8b, and 8d). This result is consistent with the work of Hong et al. (2017), wherein they argued that the SRP is responsible for the uneven warming over the Eurasian continent after the mid-1990s. Moreover, our results provide a quantitative estimation of the contribution of the SRP to the observed warming.

6. Linkage to the AMO and PDO

The link of the SRP to certain SST patterns has been a major concern in previous studies because it is expected

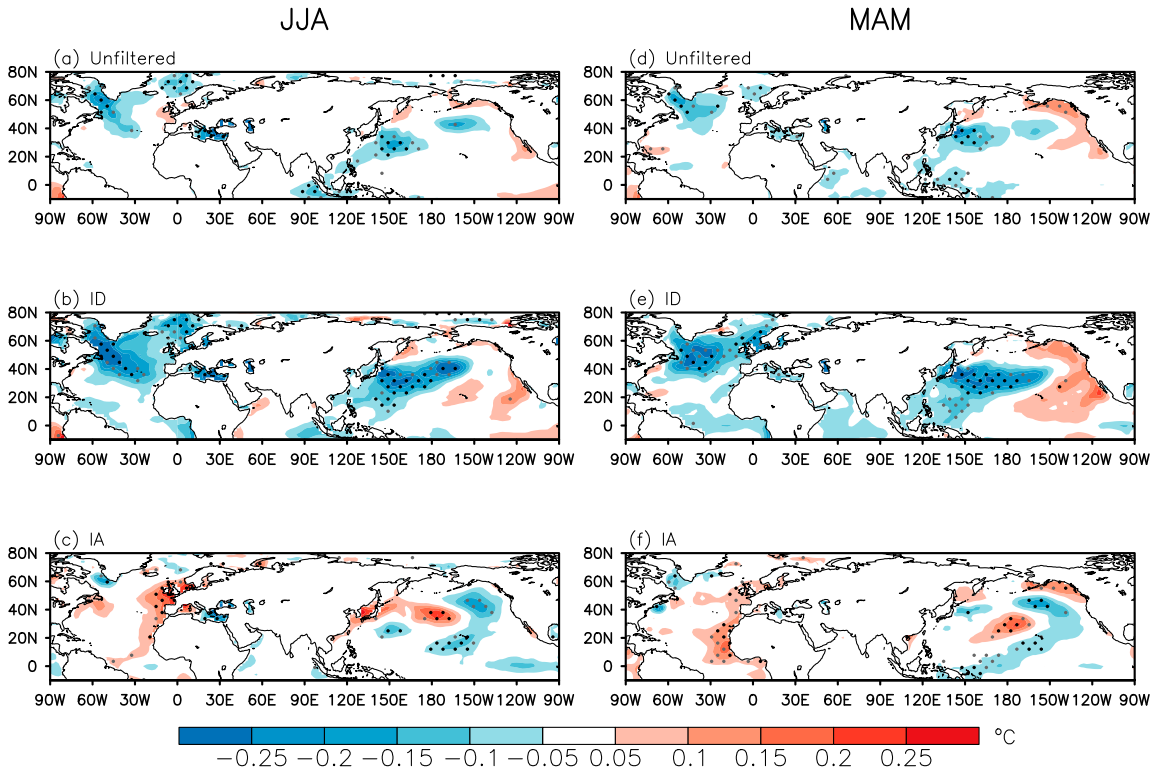

FIG. 9. (a) Regression of the summer mean SST onto the SRP index from the ERA-20C dataset for the period 1920–2010. (b),(c) As in (a), but based on the interdecadal and interannual components of the SST and the SRP index, respectively. (d)–(f) As in (a)–(c), but based on spring mean SST and summer mean SRP index. The gray and black dots indicate the 95% and 99% confidence levels based on two-tailed Student's *t* test, respectively.

that SST may provide predictability potentials for the SRP. Some studies (e.g., Ding et al. 2011) suggest that positive (negative) phases of the SRP occur preferentially in the summers preceding the peak phases of La Niña (El Niño), whereas other studies suggest that the phase of the SRP is loosely linked to SST (e.g., Lu et al. 2002) and is unpredictable on interannual time scales (e.g., Kosaka et al. 2012). Although a consensus has not been reached, the studies concerning the links between the SRP and SST have been performed extensively on interannual time scales. In contrast, it is not clear whether the variability of the SRP is linked to certain SST patterns on interdecadal time scales.

Figures 9a–c show the regressed summer mean SST onto the SRP index based on the ERA-20C dataset for the period 1920–2010. The positive phase of the SRP corresponds to the SST cooling over the North Atlantic surrounding Greenland and over the western North Pacific when the unfiltered SRP index and SST are used, but the SST anomalies in these two regions are relatively weak and statistically significant only in small regions (Fig. 9a). The negative SST anomalies are much stronger, cover larger areas, and show more statistically significant signals when the interdecadal SRP is considered. The SST pattern resembles the negative phase of the AMO (Fig. 10a) over the North Atlantic and the positive phase of the PDO (Fig. 10b) over the Pacific (Fig. 9b), implying a plausible link between the SRP and the AMO/PDO on interdecadal time scales. In contrast, when the interannual component is considered, the SRP-related SSTs show a weak horseshoe pattern in the North Pacific but do not show a well-organized pattern over the Atlantic (Fig. 9c). The results remain almost the same when the SST of the preceding spring [March–May (MAM)] is regressed onto the summer mean SRP index (Figs. 9d–f).

The correlation coefficient between the interdecadal summer mean SRP index and the interdecadal component of the summer mean AMO index is −0.24, which is much stronger than that between the unfiltered SRP index and the unfiltered AMO index (Table 4). The same analyses were performed for the summer mean SRP index and the AMO index of the preceding spring; similar results are obtained (Table 4). Although none of the above correlation coefficients exceed the 90% confidence level, these results imply that the interdecadal variations of the SRP are possibly related to the AMO. To further examine this possibility, a Monte Carlo bootstrapping technique (Efron and Tibshirani 1994) was applied to estimate the

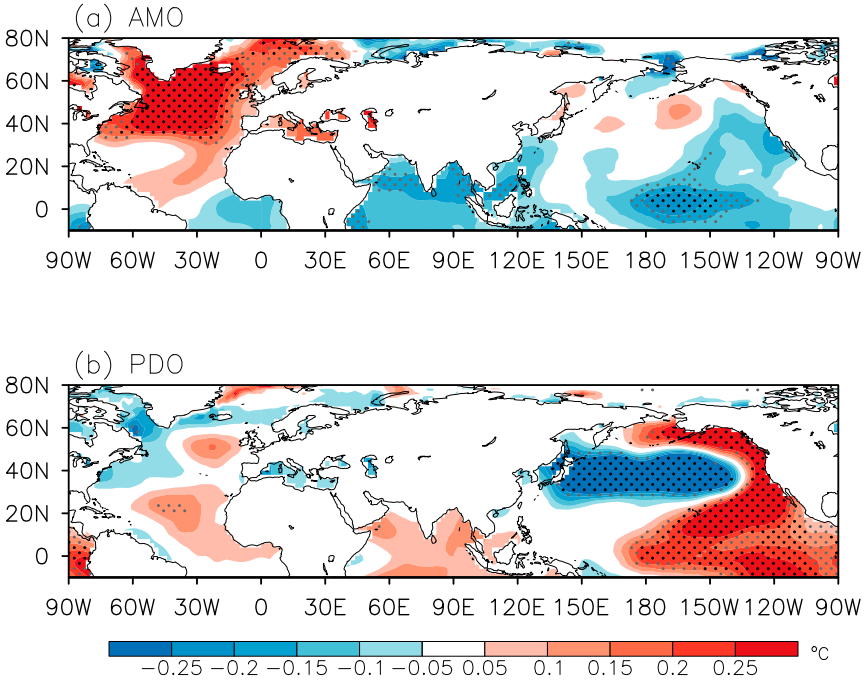

FIG. 10. Regression of the interdecadal component of the summer mean SST onto the interdecadal component of the summer mean (a) AMO index and (b) PDO index for the period 1920–2010. Gray and black dots indicate the 95% and 99% confidence levels based on two-tailed Student's *t* test, respectively.

probability density function (PDF) of the interdecadal SRP index during the positive and negative phases of the AMO, where the resampling procedure was repeated 10000 times. It reveals that the PDFs of the interdecadal SRP index in the positive and negative phases of the summer mean AMO are well separated (Fig. 11a) and that the separation is even better when the AMO index leads the SRP index by one season (Fig. 11b). Moreover, the interdecadal SRP index is significantly different from zero at the 95% confidence level, as estimated using the percentile method (Figs. 11a,b), and this is particularly clear when the spring AMO index is considered (Fig. 11b). Hence, these results suggest that the positive (negative) phases of the AMO significantly facilitate the occurrence of negative (positive) phases of the interdecadal SRP, although a significant linear relationship is not observed between the AMO and SRP indices. This information may provide some prediction potential for the interdecadal variations of the SRP.

The linear relationship between the SRP and PDO is similar to that between the SRP and AMO (Table 4), suggesting that the SRP and PDO are possibly related to each other on interdecadal time scales. Again, the Monte Carlo bootstrapping technique was employed to estimate the PDFs of the interdecadal SRP index during the positive and negative phases of the PDO. The medians of the interdecadal SRP index during the positive and negative phases of the summer mean PDO are well separated (Fig. 11c), but their PDFs are not as well separable as those based on the phases of the summer mean AMO (Figs. 11a,c). Moreover, the interdecadal SRP index is not significantly different from zero at the 95% confidence level (Fig. 11c). The separation is even worse when the PDO index leads the SRP index by one season (Fig. 11d). Therefore, these results suggest that the PDO is unlikely to be a driving factor of the interdecadal variability of the SRP.

7. Conclusions and discussion

In this study, the interdecadal variations of the SRP are investigated based on several reanalysis and observational

TABLE 4. Correlation coefficients between the original and interdecadal (left and right, separated by a slash) SRP index and the original and interdecadal summer and spring mean AMO and PDO indices during the period 1920–2010. None of the correlation coefficients exceed the 90% confidence level based on two-tailed Student's *t* test.

	AMO	PDO
JJA	−0.10/−0.24	0.10/0.26
MAM	−0.07/−0.26	0.14/0.19

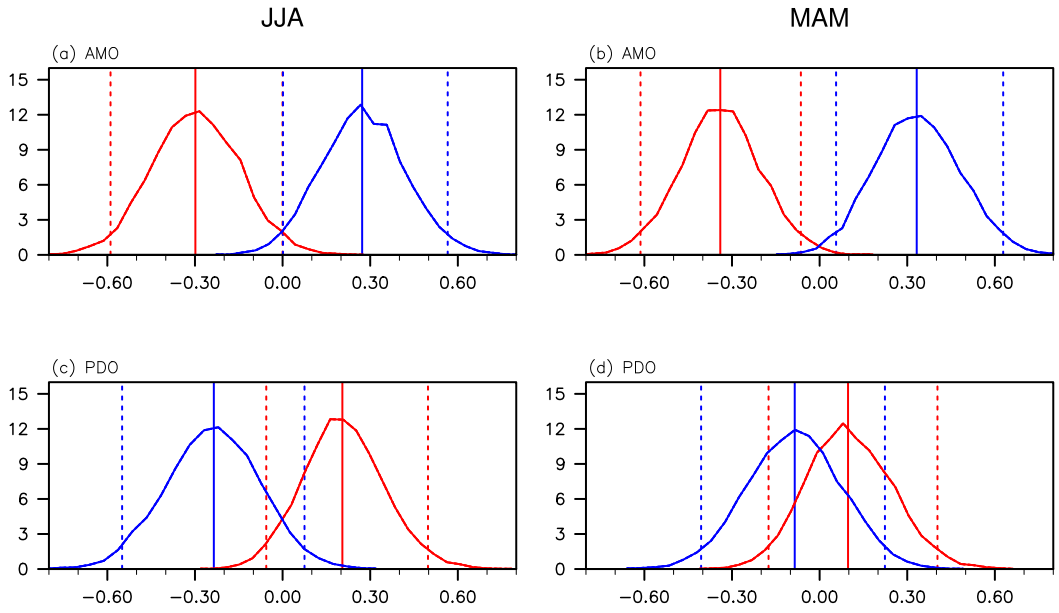

FIG. 11. PDF (curve) and median (vertical solid line) of the interdecadal SRP index estimates from 10 000 bootstrapped samples in the positive (red) and negative (blue) phases of the (a) summer mean interdecadal AMO index and (b) spring mean interdecadal AMO index. (c),(d) As in (a),(b), but for the positive (red) and negative (blue) phases of the interdecadal PDO index. The vertical dashed lines indicate the 5% and 95% percentiles. The SRP index is from the ERA-20C dataset for the period 1920–2010.

datasets. Wavelet analysis reveals that the SRP has a significant 8–16-yr and 32–64-yr variability, which is highly consistent in the different datasets (Figs. 3a–e). The interdecadal component of the SRP explains approximately 50% or more of the total variance (Table 3), suggesting its importance in the variability of the SRP. The mean value of the SRP index experiences two regime shifts, in 1972 and 1997, and a third plausible regime shift in the 1930s (Figs. 3f–j).

After extracting the interdecadal component of the SRP via a 9-yr Lanczos low-pass filter, regression analysis indicates that the interdecadal SRP not only features a clear barotropic wave train propagating along the Asian subtropical jet stream like the interannual SRP does but also features a weak northern branch of wave train emanating from the British Isles, across northern Scandinavia and the Taymyr Peninsula, to Mongolia (Figs. 4a–d). This structure is better represented in the relative vorticity field than in the geopotential height field. As a result, three barotropic anticyclonic centers over the British Isles, the Caspian Sea, and the Korean Peninsula and two cyclonic centers over eastern Europe and Mongolia are formed during the positive phase of the SRP. Overall, the structure of the interdecadal SRP is similar to that of the interannual SRP but shows much larger meridional scales, especially over eastern Europe and Mongolia, due to the existence of the northern branch of its wave train (Fig. 4).

On interdecadal time scales, the positive phase of the SRP could lead to less rainfall over western Europe, Siberia, and the southern part of China and more rainfall over eastern Europe, India, and northeastern Asia. The amount of the variance of precipitation explained by the interdecadal SRP is generally on the order of 10%–20%, despite some uncertainties (Figs. 5a–d). Meanwhile, the interdecadal SRP could result in large-scale cooling over Europe and northeastern Asia and weak warming over central Asia (Figs. 6a–d). The variance of the surface air temperature explained by the interdecadal SRP reaches up to 50% over eastern Europe, western Asia, and northeastern Asia, suggesting its crucial role in modulating the Eurasian surface air temperature on interdecadal time scales. Specifically, the association of the SRP with the decadal shift of the Eurasian summer climate in the late 1990s was investigated. Over 60% (40%) of the observed rainfall increase (reduction) over northwestern Europe (northeastern Asia) and over 40% of the observed warming over eastern Europe and northeastern Asia can be explained by the transition of the SRP from its positive to its negative phase in 1998 (Fig. 8).

The interdecadal variations of the SRP are shown to be associated with SST anomalies that resemble the AMO and PDO (Fig. 9). Although the linear relationship between the interdecadal SRP and AMO indices is insignificant during the period 1920–2010, the

estimation of the PDF of the interdecadal SRP index with respect to phases of the AMO done using a Monte Carlo bootstrapping technique suggests that the positive (negative) phase of the AMO significantly facilitates the occurrence of a negative (positive) phase of the interdecadal SRP (Figs. 11a,b). In contrast, the link between the interdecadal SRP and the PDO is much weaker (Figs. 11c,d). These results indicate that the phase of the AMO is likely to provide some prediction potential for the interdecadal variations of the SRP.

Understanding the mechanism of how the AMO influences the interdecadal variations of the SRP is crucial to support the statistical results shown in this study, but it is beyond the scope of this study. Nevertheless, a recent observational study suggests that the AMO is closely linked to a wave train over Eurasia that considerably resembles the SRP (see Fig. 9a of Si and Ding 2016). A model study also shows an SRP-like response to the Atlantic multidecadal variability (see Fig. 9a of Msadek et al. 2011). Both of these studies support our argument that the AMO is very likely a driver of the interdecadal variations of the SRP and thereby encourages us to explore the mechanism of this connection through numerical model experiments in the future.

Last but not least, the results presented in this study are based on data without removing long-term trends, but the global mean temperature has shown a clear warming trend over the past decades (e.g., Hartmann et al. 2013; Sun et al. 2017). To examine the possible sensitivity of our results to long-term trends, all analyses were repeated using detrended data (trends were estimated using the least squares method during the period 1920–2010), and the results remain almost unchanged (not shown). This lack of change suggests that the results reported in this study are unlikely to be influenced by global warming and other external forcings outside of the climate system, but likely originated from internal variability within the climate system.

Acknowledgments. We thank the three anonymous reviewers for their constructive comments that led to the improvements of the manuscript. This work was supported by the National Key Research and Development Program of China (2016YFA0600604) and the National Natural Science Foundation of China (41422501, 41661144016).

REFERENCES

Ambrizzi, T., B. J. Hoskins, and H. H. Hsu, 1995: Rossby wave propagation and teleconnection patterns in the austral winter. *J. Atmos. Sci.*, **52**, 3661–3672, doi:10.1175/1520-0469(1995)052<3661:RWPATP>2.0.CO;2.

Bretherton, C. S., M. Widmann, V. P. Dymnikov, J. M. Wallace, and I. Bladé, 1999: The effective number of spatial degrees of freedom of a time-varying field. *J. Climate*, **12**, 1990–2009, doi:10.1175/1520-0442(1999)012<1990:TENOSD>2.0.CO;2.

Chen, G., and R. Huang, 2012: Excitation mechanisms of the teleconnection patterns affecting the July precipitation in northwest China. *J. Climate*, **25**, 7834–7851, doi:10.1175/JCLI-D-11-00684.1.

——, ——, and L. Zhou, 2013: Baroclinic instability of the Silk Road pattern induced by thermal damping. *J. Atmos. Sci.*, **70**, 2875–2893, doi:10.1175/JAS-D-12-0326.1.

Chen, W., and R. Y. Lu, 2014: A decadal shift of summer surface air temperature over northeast Asia around the mid-1990s. *Adv. Atmos. Sci.*, **31**, 735–742, doi:10.1007/s00376-013-3154-4.

——, and Coauthors, 2016: Variation in summer surface air temperature over northeast Asia and its associated circulation anomalies. *Adv. Atmos. Sci.*, **33**, 1–9, doi:10.1007/s00376-015-5056-0.

Compo, G. P., and Coauthors, 2011: The Twentieth Century Reanalysis Project. *Quart. J. Roy. Meteor. Soc.*, **137**, 1–28, doi:10.1002/qj.776.

Dai, A., 2013: The influence of the inter-decadal Pacific Oscillation on US precipitation during 1923–2010. *Climate Dyn.*, **41**, 633–646, doi:10.1007/s00382-012-1446-5.

Dee, D. P., and Coauthors, 2011: The ERA-Interim reanalysis: Configuration and performance of the data assimilation system. *Quart. J. Roy. Meteor. Soc.*, **137**, 553–597, doi:10.1002/qj.828.

Ding, Q. H., and B. Wang, 2005: Circumglobal teleconnection in the Northern Hemisphere summer. *J. Climate*, **18**, 3483–3505, doi:10.1175/JCLI3473.1.

——, ——, J. M. Wallace, and G. Branstator, 2011: Tropical–extratropical teleconnections in boreal summer: Observed interannual variability. *J. Climate*, **24**, 1878–1896, doi:10.1175/2011JCLI3621.1.

Efron, B., and R. J. Tibshirani, 1994: *An Introduction to the Bootstrap.* Chapman and Hall, 456 pp.

Enomoto, T., 2004: Interannual variability of the Bonin high associated with the propagation of Rossby waves along the Asian jet. *J. Meteor. Soc. Japan*, **82**, 1019–1034, doi:10.2151/jmsj.2004.1019.

——, B. J. Hoskins, and Y. Matsuda, 2003: The formation mechanism of the Bonin high in August. *Quart. J. Roy. Meteor. Soc.*, **129**, 157–178, doi:10.1256/qj.01.211.

Harris, I., P. D. Jones, T. J. Osborn, and D. H. Lister, 2014: Updated high-resolution grids of monthly climatic observations—The CRU TS3.10 dataset. *Int. J. Climatol.*, **34**, 623–642, doi:10.1002/joc.3711.

Hartmann, D. L., and Coauthors, 2013: Observations: Atmosphere and surface. *Climate Change 2013: The Physical Science Basis*, T. F. Stocker et al., Eds., Cambridge University Press, 159–254.

Hong, X., and R. Lu, 2016: The meridional displacement of the summer Asian jet, Silk Road pattern, and tropical SST anomalies. *J. Climate*, **29**, 3753–3766, doi:10.1175/JCLI-D-15-0541.1.

——, ——, and S. Li, 2017: Amplified summer warming in Europe–west Asia and northeast Asia after the mid-1990s. *Environ. Res. Lett.*, **12**, 094007, doi:10.1088/1748-9326/aa7909.

Hoskins, B. J., and T. Ambrizzi, 1993: Rossby wave propagation on a realistic longitudinally varying flow. *J. Atmos. Sci.*, **50**, 1661–1671, doi:10.1175/1520-0469(1993)050<1661:RWPOAR>2.0.CO;2.

——, A. J. Simmons, and D. G. Andrews, 1977: Energy dispersion in a barotropic atmosphere. *Quart. J. Roy. Meteor. Soc.*, **103**, 553–567, doi:10.1002/qj.49710343802.

Hu, K., G. Huang, R. Wu, and L. Wang, 2017: Structure and dynamics of a wave train along the wintertime Asian jet and its impact on East Asian climate. *Climate Dyn.*, doi:10.1007/s00382-017-3674-1, in press.

Huang, B., and Coauthors, 2015: Extended Reconstructed Sea Surface Temperature version 4 (ERSST.v4). Part I: Upgrades and intercomparisons. *J. Climate*, **28**, 911–930, doi:10.1175/JCLI-D-14-00006.1.

Huang, G., Y. Liu, and R. Huang, 2011: The interannual variability of summer rainfall in the arid and semiarid regions of northern China and its association with the Northern Hemisphere circumglobal teleconnection. *Adv. Atmos. Sci.*, **28**, 257–268, doi:10.1007/s00376-010-9225-x.

Huang, R. H., J. L. Chen, L. Wang, and Z. D. Lin, 2012: Characteristics, processes, and causes of the spatio-temporal variabilities of the East Asian monsoon system. *Adv. Atmos. Sci.*, **29**, 910–942, doi:10.1007/s00376-012-2015-x.

——, Y. Liu, and T. Feng, 2013: Interdecadal change of summer precipitation over eastern China around the late-1990s and associated circulation anomalies, internal dynamical causes. *Chin. Sci. Bull.*, **58**, 1339–1349, doi:10.1007/s11434-012-5545-9.

Iwao, K., and M. Takahashi, 2008: A precipitation seesaw mode between northeast Asia and Siberia in summer caused by Rossby waves over the Eurasian continent. *J. Climate*, **21**, 2401–2419, doi:10.1175/2007JCLI1949.1.

Kalnay, E., and Coauthors, 1996: The NCEP/NCAR 40-Year Reanalysis Project. *Bull. Amer. Meteor. Soc.*, **77**, 437–471, doi:10.1175/1520-0477(1996)077<0437:TNYRP>2.0.CO;2.

Kobayashi, S., and Coauthors, 2015: The JRA-55 Reanalysis: General specifications and basic characteristics. *J. Meteor. Soc. Japan*, **93**, 5–48, doi:10.2151/jmsj.2015-001.

Kosaka, Y., H. Nakamura, M. Watanabe, and M. Kimoto, 2009: Analysis on the dynamics of a wave-like teleconnection pattern along the summertime Asian jet based on a reanalysis dataset and climate model simulations. *J. Meteor. Soc. Japan*, **87**, 561–580, doi:10.2151/jmsj.87.561.

——, J. S. Chowdary, S.-P. Xie, Y.-M. Min, and J.-Y. Lee, 2012: Limitations of seasonal predictability for summer climate over East Asia and the northwestern Pacific. *J. Climate*, **25**, 7574–7589, doi:10.1175/JCLI-D-12-00009.1.

Krishnan, R., and M. Sugi, 2001: Baiu rainfall variability and associated monsoon teleconnections. *J. Meteor. Soc. Japan*, **79**, 851–860, doi:10.2151/jmsj.79.851.

Lau, K. M., K. M. Kim, and S. Yang, 2000: Dynamical and boundary forcing characteristics of regional components of the Asian summer monsoon. *J. Climate*, **13**, 2461–2482, doi:10.1175/1520-0442(2000)013<2461:DABFCO>2.0.CO;2.

Liebmann, B., and C. A. Smith, 1996: Description of a complete (interpolated) OLR dataset. *Bull. Amer. Meteor. Soc.*, **77**, 1275–1277.

Lu, R. Y., J. H. Oh, and B. J. Kim, 2002: A teleconnection pattern in upper-level meridional wind over the North African and Eurasian continent in summer. *Tellus*, **54A**, 44–55, doi:10.3402/tellusa.v54i1.12122.

——, B. Dong, and H. Ding, 2006: Impact of the Atlantic multidecadal oscillation on the Asian summer monsoon. *Geophys. Res. Lett.*, **33**, L24701, https://doi.org/10.1029/2006GL027655.

Mantua, N. J., S. R. Hare, Y. Zhang, J. M. Wallace, and R. C. Francis, 1997: A Pacific interdecadal climate oscillation with impacts on salmon production. *Bull. Amer. Meteor. Soc.*, **78**, 1069–1079, doi:10.1175/1520-0477(1997)078<1069:APICOW>2.0.CO;2.

Msadek, R., C. Frankignoul, and L. Z. X. Li, 2011: Mechanisms of the atmospheric response to North Atlantic multidecadal variability: A model study. *Climate Dyn.*, **36**, 1255–1276, doi:10.1007/s00382-010-0958-0.

Nakamura, H., and T. Fukamachi, 2004: Evolution and dynamics of summertime blocking over the Far East and the associated surface Okhotsk high. *Quart. J. Roy. Meteor. Soc.*, **130**, 1213–1233, doi:10.1256/qj.03.101.

Park, T.-W., C.-H. Ho, and S. Yang, 2011: Relationship between the Arctic Oscillation and cold surges over East Asia. *J. Climate*, **24**, 68–83, doi:10.1175/2010JCLI3529.1.

Piao, J., W. Chen, K. Wei, Y. Liu, H. F. Graf, J.-B. Ahn, and A. Pogoreltsev, 2017: An abrupt rainfall decrease over the Asian inland plateau region around 1999 and the possible underlying mechanism. *Adv. Atmos. Sci.*, **34**, 456–468, doi:10.1007/s00376-016-6136-5.

Poli, P., and Coauthors, 2016: ERA-20C: An atmospheric reanalysis of the twentieth century. *J. Climate*, **29**, 4083–4097, doi:10.1175/JCLI-D-15-0556.1.

Saeed, S., W. A. Müller, S. Hagemann, and D. Jacob, 2011: Circumglobal wave train and the summer monsoon over northwestern India and Pakistan: The explicit role of the surface heat low. *Climate Dyn.*, **37**, 1045–1060, doi:10.1007/s00382-010-0888-x.

——, N. Van Lipzig, W. A. Müller, F. Saeed, and D. Zanchettin, 2014: Influence of the circumglobal wave-train on European summer precipitation. *Climate Dyn.*, **43**, 503–515, doi:10.1007/s00382-013-1871-0.

Sato, N., and M. Takahashi, 2006: Dynamical processes related to the appearance of quasi-stationary waves on the subtropical jet in the midsummer Northern Hemisphere. *J. Climate*, **19**, 1531–1544, doi:10.1175/JCLI3697.1.

Schlesinger, M. E., and N. Ramankutty, 1994: An oscillation in the global climate system of period 65–70 years. *Nature*, **367**, 723–726, doi:10.1038/367723a0.

Si, D., and Y. Ding, 2016: Oceanic forcings of the interdecadal variability in East Asian summer rainfall. *J. Climate*, **29**, 7633–7649, doi:10.1175/JCLI-D-15-0792.1.

Song, L., L. Wang, W. Chen, and Y. Zhang, 2016: Intraseasonal variation of the strength of the East Asian trough and its climatic impacts in boreal winter. *J. Climate*, **29**, 2557–2577, doi:10.1175/JCLI-D-14-00834.1.

Sun, X., G. Ren, W. Xu, Q. Li, and Y. Ren, 2017: Global land–surface air temperature change based on the new CMA GLSAT data set. *Sci. Bull.*, **62**, 236–238, doi:10.1016/j.scib.2017.01.017.

Sutton, R. T., and B. Dong, 2012: Atlantic Ocean influence on a shift in European climate in the 1990s. *Nat. Geosci.*, **5**, 788–792, doi:10.1038/ngeo1595.

Takaya, K., and H. Nakamura, 2001: A formulation of a phase-independent wave-activity flux for stationary and migratory quasigeostrophic eddies on a zonally varying basic flow. *J. Atmos. Sci.*, **58**, 608–627, doi:10.1175/1520-0469(2001)058<0608:AFOAPI>2.0.CO;2.

Torrence, C., and G. P. Compo, 1998: A practical guide to wavelet analysis. *Bull. Amer. Meteor. Soc.*, **79**, 61–78, doi:10.1175/1520-0477(1998)079<0061:APGTWA>2.0.CO;2.

Wang, H., B. Wang, F. Huang, Q. Ding, and J.-Y. Lee, 2012: Interdecadal change of the boreal summer circumglobal teleconnection (1958–2010). *Geophys. Res. Lett.*, **39**, L12704, doi:10.1029/2012GL052371.

Willmott, C., and K. Matsuura, 2014: Terrestrial air temperature: 1900–2010 gridded monthly time series, version 3.01. NCAR–UCAR/University of Delaware Climate Data Guide, http://climate.geog.udel.edu/~climate/.

Wu, B., J. Lin, and T. Zhou, 2016: Interdecadal circumglobal teleconnection pattern during boreal summer. *Atmos. Sci. Lett.*, **17**, 446–452, doi:10.1002/asl.677.

Wu, R., 2002: A mid-latitude Asian circulation anomaly pattern in boreal summer and its connection with the Indian and East Asian summer monsoons. *Int. J. Climatol.*, **22**, 1879–1895, doi:10.1002/joc.845.

Yasui, S., and M. Watanabe, 2010: Forcing processes of the summertime circumglobal teleconnection pattern in a dry AGCM. *J. Climate*, **23**, 2093–2114, doi:10.1175/2009JCLI3323.1.

Zhang, R., 2015: Changes in East Asian summer monsoon and summer rainfall over eastern China during recent decades. *Sci. Bull.*, **60**, 1222–1224, doi:10.1007/s11434-015-0824-x.

Zhu, Y., H. Wang, W. Zhou, and J. Ma, 2011: Recent changes in the summer precipitation pattern in east China and the background circulation. *Climate Dyn.*, **36**, 1463–1473, doi:10.1007/s00382-010-0852-9.

——, T. Wang, and H. Wang, 2016: Relative contribution of the anthropogenic forcing and natural variability to the interdecadal shift of climate during the late 1970s and 1990s. *Sci. Bull.*, **61**, 416–424, doi:10.1007/s11434-016-1012-3.